Hydrodesulfurization of 4,6-dimethyldibenzothiophene over NiMo sulfide catalysts supported on meso-microporous Y zeolite with different mesopore sizes

Wenwu Zhou[a,b,*], Qiang Wei[b], Yasong Zhou[b,*], Meifang Liu[b], Sijia Ding[b], Qi Yang[b]

[a] School of Chemistry and Chemical Engineering, Xi'an University of Science and Technology, Xi'an, 710054, PR China
[b] State Key Laboratory of Heavy Oil Processing, China University of Petroleum, Beijing 102249, PR China

ABSTRACT

MY-x series zeolites with different mesopore diameters were successfully synthesized via a hydrothermal synthesis procedure and the corresponding NiMo/HMY-x series hydrodesulfurization(HDS) catalysts were prepared via incipient co-impregnation method. The synthesized samples were characterized by both wide and small angle XRD, N_2 adsorption-desorption isotherms, pyridine adsorbed FTIR (Py-FTIR), ^{27}Al MAS NMR, H_2-TPR, HRTEM and XPS. The results show that the synthesized samples exhibit wide opened mesopores of varying sizes with well crystallized pore walls. The introduction of mesopores caused a slight decline in the interaction between active metals and support (MSI) in the corresponding catalysts, generating higher stacking numbers and a shorter slab lengths among MoS_2 crystals on the corresponding catalyst and favoring both the dispersion and sulfidation of Mo species, particularly favoring the formation of both active edge sites and highly active corner active sites. The reaction network for 4,6-DMDBT HDS over NiMo/HMY-x series catalysts is proposed, and HDS selectivity is found to be related to mesopore size. More specifically, HYD activity is linearly correlated to the number of Mo atoms located along the edge sites of MoS_2 crystals, and DDS activity is linearly correlated with the number of Mo atoms located at the corner sites of MoS_2 crystals. Finally, the active corner sites are approximately 10 times more active than active edge sites.

1. Introduction

The complete removal of sulfur compounds from petroleum feedstock and especially from inferior diesel remains a global environmental problem due to negative impacts on the atmosphere and human health resulting from their combustion [1–3]. With the establishment of increasingly stricter government specifications, the production of ultraclean diesel is attracting more attention internationally [4,5]. Hydrodesulfurization(HDS) is considered the most effective and most commonly used industrial process for producing ultralow sulfur diesels ($< 10\,\mu g\,g^{-1}$), for which the design and preparation of catalysts of high HDS performance are believed to be central factors [6–8]. γ-Al_2O_3 is often used as the commercial HDS catalyst support owing to its low price, relatively high surface area, high level of stability and excellent formability [9,10]. However, it is becoming more difficult to produce diesels meeting strict specifications of diesel quality from increasingly lower quality raw diesels using commercial HDS catalysts [11–13]. Therefore, new support materials for high efficient HDS catalysts must

be identified [14–16]. The acidity levels and pore structures of support materials are considered to the most important features that shape the properties and performance of related HDS catalysts [17,18]. As highly refractory organosulfur compounds such as 4,6-DMDBT are the most difficult to remove through the HDS process, and as kinetic studies of 4,6-DMDBT HDS over NiMo/Al_2O_3 catalyst show that the cleavage of C–S bonds constitutes a rate-determining step [3,9,19,20], zeolites exhibiting high levels of cracking activity have been used as support or co-support materials for HDS catalysts in recent years [2,21–34]. Of the zeolites that have been examined, Y zeolite is the most suitable for the removal of highly refractory organosulfur compounds such as 4,6-DMDBT owing to its microporosity levels, which are equivalent to the size of organosulfur molecules according to density functional theory calculations [2]. Pérot [21] proposed that 4,6-DMDBT can form an isomerization pathway (ISO pathway), which is completely different from the conventional direct desulfurization pathway (DDS pathway) and hydrogenation desulfurization pathway (HYD pathway), over NiMo/USY and Mo/USY catalysts. Furthermore, the isomerization of

4,6-DMDBT into less refractory organosulfur compounds-3,6-DMDBT and 3,7-DMDBT, makes the ultra-deep HDS process more easily. Our previous studies [28,29] also show that 4,6-DMDBT undergoes HDS mainly via the ISO pathway over NiMo/2GaY-ASA-A and NiMo/USNiY catalysts and this can be attributed to acid properties of Y zeolite. However, from these studies, we also found that micropores of Y zeolites have a negative impact on the deposition and dispersion of active metals and on the diffusion of reactant molecules. Several efforts have been made to overcome diffusion limitations resulting from the solely existence of micropores with a diameter of roughly 0.73 nm. Pérez-Ramírez [35] and coauthors developed a post-synthetic method for obtaining hierarchical Y zeolites and studied the Knoevenagel condensation of benzaldehyde with malononitrile. Their results show that catalytic activity levels of hierarchical Y zeolite are up to 10 times greater than those of Y zeolites, as the existence of a secondary mesopore network enhances both the mass transportation of reactants and the accessibility of active sites. Zhu's research group [33] developed a strategy for synthesizing hierarchical mesoporous zeolites through the elaborate design of mesoscale cationic surfactants, and they found that the adsorptive capacity of the synthesized sample to be four times greater for bulky N-nitrosonornicotine than for NaY zeolite due to the former's hierarchical mesostructure. Shen and coauthors [34] proposed a means of obtaining hierarchical Y zeolites without the use of an organic template, and they found the catalytic performance of the related catalyst to be enhanced and that gasoline yields gernerated from the catalytic cracking of heavy oil increase with the elimination of the mass transportation of bulky reactants and products. Xiao and colleagues [2] employed *N,N*-dimethyl-*N*-octadecyl-*N*-(3-triethoxysilylpropyl) ammonium cation as a mesoscale template for synthesizing a hierarchical Y zeolite and used the synthesized hierarchical Y zeolite to support the Pd/HY-M HDS catalyst for the first time. The authors show that combining mesopores with large micropores(composed of 12-membered ring) in HY-M enhances the catalytic performance of 4,6-DMDBT for the related HDS catalyst. These studies show that the porosity of support materials is of central importance to the catalytic performance of the related catalysts. However, the mesopores of all hierarchical Y zeolites described in the mentioned works are disordered, rendering it impossible to study pore confinement effects of related HDS catalysts in cases of ultra-deep hydrodesulfurization. Moreover, the synthesis of highly ordered mesoporous Y zeolites remains challenging.

It is widely accepted that the mesopore diameter affects the morphology of the active phase and the catalytic performance of bimetallic NiMo supported HDS catalysts. We have recently recommended the use of a scaled-up synthetic approach to the continuous synthesis of narrow dispersed mesoporous Y zeolite from normal inorganic aluminosilicates [36], and it is believed that methyl groups located in the 4- and 6-positions cause steric hindrance in 4,6-DMDBT during HDS reactions. Thus, the adsorption of DBT and 4,6-DMDBT across narrowly dispersed mesoporous Y zeolites with different mesopore sizes has also been investigated recently. It has been found that samples with narrowly dispersed mesopores exhibit the superior adsorption capacities for both DBT and 4,6-DMDBT through their elimination of diffusion limitations and limited steric hindrance effects. However, a number of questions in this area remain. The synthesis of narrowly dispersed mesoporous Y zeolites renders it possible to investigate pore confinement effects of NiMo supported on mesoporous Y zeolite catalysts. The following questions remain. (1) How do the diameters of mesopores of mesoporous Y zeolites affect the morphology of the active phase of a NiMo supported catalyst? (2) Does a specific optical mesopore diameter support the removal of highly refractory organosulfur compounds such as 4,6-DMDBT? (3) If so, what mesopore diameter is optical? In the present study, mesoporous Y zeolites with mesopore diameters of 4 nm, 6 nm and 8 nm were successfully synthesized using our previously developed synthetic strategy [36]. Corresponding NiMo-supported HDS catalysts were prepared and carefully characterized to investigate the relationship between mesopore diameters and the active phase

morphology. Finally, HDS reactions of 4,6-DMDBT for corresponding catalysts were initiated to obtain an optical mesopore diameter of ultra-deep HDS catalysts presenting higher levels of activity for the production of ultra-low sulfur petroleum fractions.

2. Experimental

2.1. Synthesis of samples

Mesoporous Y zeolites with different mesopore diameters were continuously synthesized using our previously developed method [36,37]. In a typical synthesis, measured amounts of sodium hydroxide (Beijing Modern Oriental Fine Chemical Co. Ltd., no less than 99.8%), sodium aluminate (Guangfu Fine Chemical Co. Ltd. no less than 99.8%), and sodium silica (28 wt % SiO_2, 9.1 wt % Na_2O, and 62.9 wt % H_2O) were suspended in measured amounts of deionized water at 5 °C with vigorous agitation. We then dissolved aluminum sulfate (Beijing Modern Oriental Fine Chemical Co. Ltd., no less than 99.8%) in 20 g of deionized water and added this solution to the suspension dropwise at 5 °C under continuous agitation. The composition of the colloidal obtained was measured as 7.5:1:16:240 ($Na_2O/Al_2O_3/SiO_2/H_2O$). The resulting colloidal was aged at 30 °C for roughly 20 h and was hydrothermally treated at 65 °C for 36 h in a Teflon autoclave. The autoclave was then cooled to 30 °C under air flow, and a solution composed of 5 g of CTAB (Aladdin, no less than 99.9%) as an organic template, 3–6.5 mL of 1,3,5-trimethybenzene (TMB) (Aladdin, no less than 99.9%) as a swelling agent, 1 g of sodium hydroxide, 10 mL of butyl alcohol (Beijing Modern Oriental Fine Chemical Co. Ltd., no less than 99.8%) as a co-solvent and 20 g of tetraethylorthosilicate (TEOS) (Guangfu Chemical Co. Ltd. no less than 99.8%) in 20 g of deionized water self-assembled for 30 min was added to the colloidal. Then the colloidal was first temperature programmed and crystallized at 70 °C for 24 h, then at 95 °C for 20 h and finally at 105 °C for 2 h. The obtained product was filtrated, dried and calcinated. The final samples were labeled MY-x, where x is the mesopore diameter (in nm) of the synthesized samples.

2.2. Preparation of catalysts

The synthesized MY-x series mesoporous Y zeolites with different mesopore diameters were first ion-exchanged by NH_4NO_3 solution with molar concentrations of 1 M three times following the procedure described in our previous works [29,38,39], and the ion-exchanged samples were labeled as HMY-x. The obtained HMY-x samples were pelleted and crushed into particles with diameters of 0.59 to 0.84 mm. The aqueous solution containing calculated amounts of nickel nitrate hexahydrate(Ni(NO$_3$)$_2$·6H$_2$O; Beijing Modern Oriental Fine Chemical Co. Ltd., no less than 99.8%) and ammonium heptamolybdate tetrahydrate((NH$_4$)$_6$Mo$_7$O$_{24}$·4H$_2$O; Beijing Modern Oriental Fine Chemical Co. Ltd., no less than 99.8%) was impregnated to the obtained particles via the incipient wetness co-impregnation method, and samples obtained were first dried in air for no less than 12 h at room temperature and then fully dried in an oven at 120 °C for 6 h. Finally, the dried catalysts were calcined in a muffle furnace under air flow at 550 °C for 5 h, and the obtained catalysts were labeled as NiMo/HMY-x. Metal oxide content in the NiMo/HMY-x series catalysts was unified (with an NiO loading of 4 wt.% and an MoO$_3$ loading of 12 wt.%).

2.3. Material characterization

Wide- (WA) and small-angle (SA) X-ray diffraction (XRD) patterns of the synthesized mesoporous Y zeolites with different mesopore diameters were recorded on a PANalytical Advance powder diffractometer at room temperature at Cu Kα radiation (λ = 1.5406 Å) and at 2θ intervals of 5~35° (WA) and 0.5~5° (SA), respectively. The crystalline phase of the synthesized samples was identified from XRD patterns observed in referred to the standard Powder Diffraction File (PDF# 38-

0239) card available at the JCPDS-ICDD library.

Textural characteristics of the synthesized mesoporous Y zeolites with different mesopore diameters were obtained using a Micromeritics ASAP 2010 volumetric analyzer at $-196\,°C$ by using N_2 as an adsorbate, and adsorption-desorption isotherms were recorded. Prior to this, the tested samples were fully degassed at $300\,°C$ for 6 h within a vacuum. The surface areas of the synthesized samples were measured using the Brunauer-Emmett-Teller (BET) equation within a relative pressure(P/P_0) range of $0.05\sim0.3$; pore volumes of the synthesized samples were obtained via the Barrett-Joyner-Halenda(BJH) method according to the amount of N_2 adsorbed at a relative pressure level of 0.99; and the mesopore diameter distribution of the synthesized samples was obtained via the nonlocal density functional theory(NLDFT) method [40] according to the adsorption isotherm.

Acidity properties of the synthesized mesoporous Y zeolites with different mesopore diameters and corresponding NiMo/HMY-x series catalysts were tested by pyridine adsorbed Fourier transform infrared spectroscopy (Py-FTIR) using a Magna 560 FT-IR analyzer and using pyridine as a probe molecule under vacuum conditions. Levels measured from Brönsted acid sites (BAS) and Lewis acid sites (LAS) were quantified according to the intensity levels of the individual IR bands at roughly 1543 and $1453\,cm^{-1}$, respectively, using molar extinction coefficients in the literature [41].

Solid state ^{27}Al magic angle spinning nuclear magnetic resonance (^{27}Al MAS NMR) spectra of the synthesized MY-x series zeolites were recorded using a Bruker Advance 300 instrument. The ^{27}Al chemical shift was referenced to a 0.1 M aqueous solution of $AlCl_3$.

H_2 temperature programmed reduction(H_2-TPR) profiles of the NiMo/HMY-x series catalysts were recorded using a Micromeritics AutoChem II 2920 automatic analyzer. Prior to this, the tested catalysts were pretreated in a mixture of Ar and air flow (v:v = 3:1) at $550\,°C$ for an hour and then cooled to $120\,°C$ in Ar flow. Reduction gas composed of 5% H_2 and 95% Ar (in volume) with a flow rate of $30\,mL\,min^{-1}$ was then feed to the examined sample, while the temperature of the furnace was programmed to increase to $1000\,°C$ at a heating rate of $10\,°C\,min^{-1}$. The H_2 consumption rate was simultaneously recorded using a TCD detector.

The oxide NiMo/HMY-x series catalysts were sulfided with a solution of 2 wt.% CS_2 dissolved in cyclohexane in a fixed bed reactor at $320\,°C$ for 5 h. Immediately following the sulfidation process, the reactor was sealed and transferred to a glove box filled with Ar as protection atmosphere, and then the sulfided catalysts were carefully unloaded and suspended in cyclohexane after being cooled to room temperature.

The sulfided catalysts were characterized using a Philips Tecnai G2 F20 instrument, and HRTEM images of the characterized catalysts were gernerated with an electron voltage of 200 kV. The average lengths and average stacking numbers of MoS_2 crystals of each catalyst were calculated according to statistical results by counting at least 400 MoS_2 slabs using the following equations according to the related literatures [10,28,42]:

Average slab length: $\overline{L} = \dfrac{\sum_{i=1}^{n} n_i l_i}{\sum_{i=1}^{n} n_i}$ (1)

Average stack number: $\overline{N} = \dfrac{\sum_{i=1}^{n} n_i N_i}{\sum_{i=1}^{n} n_i}$ (2)

For these two equations, l_i denotes the length of the slab in Å, n_i denotes the number of slabs with a slab length of l_i, and N_i denotes the number of layers found in slab i. Both fractions of Mo atoms located along the edge sites of MoS_2 slabs(f_{Moe}) and the Mo atoms located in corner sites of MoS_2 slabs (f_{Moc}) were carefully calculated using the following equations according to the relevant literatures [13,43–47]:

$f_{Moe} = \dfrac{Mo_{edge}}{Mo_{total}} = \dfrac{\sum_{i=1}^{t} 6(n_i-2)}{\sum_{i=1}^{t} (3n_i^2-3n_i + 1)}$ (3)

$f_{Moc} = \dfrac{Mo_{corner}}{Mo_{total}} = \dfrac{6}{\sum_{i=1}^{t} (3n_i^2-3n_i + 1)}$ (4)

$\dfrac{f_{Moe}}{f_{Moc}} = \dfrac{Mo_{edge}}{Mo_{corner}} = \dfrac{5\overline{L}}{3.2-3/2}$ (5)

$D_{Mo} = f_{Moe} + f_{Moc} = \dfrac{\sum_{i=1}^{t} 6(n_i-1)}{\sum_{i=1}^{t} (3n_i^2-3n_i + 1)}$ (6)

where Mo_{edge}, Mo_{corner} and Mo_{total} respectively denote the number of Mo atoms located along the edge sites of Ni promoted MoS_2 slabs, the number of Mo atoms located at corner sites of Ni promoted MoS_2 slabs and the total number of Mo atoms found in the Ni- promoted MoS_2 slabs; n_i denotes the number of Mo atoms found along one edge of an individual Ni promoted MoS_2 slab calculated from its length ($L = 3.2(2n_i - 1)$Å); and t denotes the total number of Ni- promoted MoS_2 slabs determined from at least 400 Ni promoted MoS_2 slabs.

An X-ray photoelectron spectroscopy (XPS) characterization of the sulfide catalysts was carried out using a VG ESCA Lab 250 spectrometer. Spectra were obtained via monochromatic Al Kα radiation ($h\nu = 1486.6\,eV$, 150 W). Prior to the test, sulfide catalysts were suspended in cyclohexane to prevent oxidation. The C 1 s peak with a binding energy of 284.6 eV and the Al 2p peak with a binding energy level of 74.6 eV were used to calibrate the binding energy scale.

2.4. Catalytic performance evaluation

The catalytic performance of the prepared catalysts was evaluated on a fixed-bed reactor with an 8 mm inner diameter and of 200 mm in length. We diluted 1.0 g of the tested catalyst with a particle size of 20–40 mesh to 2 mL using quartz sand of the same particle size, and we loaded this onto the above described reactor. Before the assessment, the catalyst was treated under air flow at $300\,°C$ for 2 h, and it was then sulfide using a CS_2 cyclohexane solution with a mass concentration of 2 wt.% at $320\,°C$ at a total pressure level of 4 MPa in a H_2 flow and with a liquid hourly space velocity (LHSV) of $10\,h^{-1}$ and a H_2:Oil ratio of 120 (v:v) for 6 h. The solution was then pumped to the reactor by an SZB-2 double-piston minim pump. The reactor temperature was decreased to the reaction temperature after the catalyst was sulfided with the protection of the CS_2 cyclohexane solution, and then a 4,6-DMDBT cyclohexane solution with a 4,6-DMDBT concentration of 0.5 wt.% was pumped to the reactor using an Eldex plunger pump with a total pressure level of 4 MPa, with a weight hourly space velocity (WHSV) in the range of 10-160 h^{-1}, and with a H_2/Oil ratio of 120 (v:v) at a reaction temperature of 280–310 °C. After a stabilization period of 5 h, the liquid reaction products were carefully collected and immediately off-line analyzed on an Agilent 4890D gas chromatograph equipped with a 60 m capillary Rtx-1 column (0.25 mm, RESREK) to quantify the concentrations of 4,6-DMDBT. The N_2 pressure level of the column was set to 0.3 MPa, and the N_2 flow velocity was set to $30\,mL\cdot min^{-1}$. After this was maintained at $50\,°C$ for 1 min, the column temperature was increased from $50\,°C$ to $320\,°C$ at a heat rate of $15\,°C\,min^{-1}$. To identify each compound in the liquid products and to characterize the HYD, DDS and the ISO pathway activities of each evaluated catalyst, the collected liquid products were analyzed offline using a Finnigan Trace GC–MS consisting of a Trace Ultral Gas Chromatograph (60 m-0.25 mm-0.5 μm) capillary column and an MS detector HP 5973.

3. Results and discussion

3.1. X-ray diffraction

MY-x zeolites with different mesopore diameters were hydrothermally synthesized using a self-assembled SiO_2@CTAB swelled by different amounts of 1,3,5-trimethylbenzene (TMB) as a mesopore structure directing agent with a pH of roughly 13 at 95 °C. Fig. 1 displays the wide-angle (WA) XRD patterns of the synthesized MY-x series
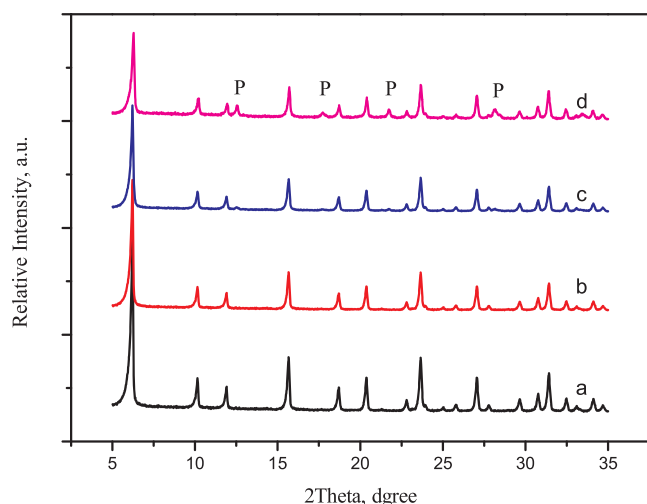
Fig. 1. WA XRD patterns of the synthesized MY-x series samples: (a) MY-0, (b) MY-4, (c) MY-6 and (d) MY-8.

zeolites.

All of the synthesized samples exhibit typical diffraction characteristics of zeolite Y, indicating that the faujasite unit cell remained intact after the introduction of mesopores. However, we found conspicuous differences in both diffraction peak widths and the diffraction peak intensities between the synthesized samples: samples MY-4, MY-6 and MY-8 exhibit much broader diffraction peak widths and much lower diffraction intensities than sample MY-0, and with an increase in mesopore diameter, the diffraction peak width further broadens, and the diffraction peak intensity level further decreases. As peak width is inversely proportional to crystal size and as peak intensity is proportional to crystallinity, we can conclude that the MY-4, MY-6 and MY-8 samples are constructed from nanocrystalline Y zeolites with lower levels of crystallinity. This decrease in crystal size and crystallinity and increase in mesopore diameter can be attributed to a decrease in the crystal thickness of mesopore walls resulting from SiO_2@CTAB micelles preventing the crystalization of Y zeolites. For sample MY-8, new diffraction peaks emerge at 2θ degree values of roughly 12.5°, 17.7°, 21.7° and 28.1° that can be assigned to the P zeolite, indicating that the presence of excessive amounts of swelling agent is not conducive to the synthesis of pure Y zeolites. WA XRD patterns of the prepared NiMo/HMY-x series catalysts (in their oxide form) are shown in Fig. S1. The results clearly show an absence of diffraction peaks attributed to either NiO or MoO_3 species, suggesting the presence of relatively high levels of dispersion among NiO and MoO_3 along surfaces of the HMY-x series samples. Following the deposition of NiO and MoO_3, the intensity of all diffraction peaks decreased profoundly. Especially for sample NiMo/

HMY-0, the intensity of diffraction peaks declined by approximate 60~70% relative to levels for sample MY-0. Small angle (SA) XRD patterns of the synthesized samples are shown in Fig. S2. The results clearly show that sample MY-0 did not generate any diffraction peaks within a 2θ range of 0.5-5°, indicating that sample MY-0 did not gernerate ordered mesopores. Samples MY-4, MY-6 and MY-8, on the other hand, gernerated wide diffraction peaks with 2θ degree values of 0.7-0.8°, denoting the presence of short-ordered mesopores with dispersed mesopore diameters. The 2θ degree of the diffraction peaks did not change considerably with an increase in mesopore diameter, and according to the Bragg equation, the distance between the two adjacent lattice points remained nearly unchanged. Thus, we observed a decrease in the thickness of the crystallized mesopore wall with an increase in mesopore diameter. The width of the MY-x series samples broadened with the mesopore diameter, revealing the presence of a more diversified distance distribution between the two adjacent lattice points. Futhermore, the intensity of the diffraction peaks increased with mesopore diameters, showing that higher ordered mesostructures or more abundant mesostructures resulting from the size of the SiO_2@CTAB micelle could match the size of Y precursors better after swelling to the proper size [36,37].

3.2. N_2 adsorption-desorption isotherms

The textural properties of the synthesized samples were characterized by N_2 physical adsorption-desorption, and the corresponding isotherms are displayed in Fig. S3. The results clearly show that all of the synthesized MY-x samples except for sample MY-0 present a typical IV isotherm with capillary condensation occurring at a relative pressure range of 0.45-0.8 with a type H2 hysteresis loop, indicating the presence of ink-bottle like mesopores in the synthesized MY-x series samples. With an increase in mesopore diameter, the hysteresis loop expands, suggesting an increase in mesopore volume. Specific pore volumes, surface areas and mesopore diameters were calculated using the methods described in the experimental section, and the corresponding results are summarized in Table 1. It is evident that specific surface areas of the synthesized MY-x series samples are almost identical, while mesopore surfaces of the synthesized MY-x series samples increase in the following order: MY-0 ($74 \, m^2 \, g^{-1}$) < < MY-4 ($228 \, m^2 \, g^{-1}$) < MY-6 ($274 \, m^2 \, g^{-1}$) < MY-8 ($326 \, m^2 \, g^{-1}$). Both the total pore volume and the mesopore volume of the synthesized MY-x series samples increased with the mesopore diameter. Accordingly, we found almost no mesopores in sample MY-0, and we measuered the mesopore diameters of samples MY-4, MY-6 and MY-8 as 4.1 nm, 6.0 nm and 7.6 nm, respectively. The pore diameter distribution of the synthesized MY-x series samples obtained from the adsorption isotherm are displayed in Fig. 2, which clearly shows the narrowly dispersed mesopore size distributions of samples MY-4, MY-6 and MY-8. It can also be concluded from Fig. 2 that the mesopore size distribution broadened

Table 1
Textural properties of the synthesized mesoporous MY-x zeolites and NiMo/HMY-x series catalysts.

Samples	NiO[a] (%)	MoO$_3$[a] (%)	S$_{BET}$[b] ($m^2 \, g^{-1}$)	S$_{meso}$ ($m^2 \, g^{-1}$)	V$_{total}$[c] ($cm^3 \, g^{-1}$)	V$_{meso}$ ($cm^3 \, g^{-1}$)	D (nm)	
							BJH	NLDFT
MY-0	–	–	628	74	0.48	0.08	–	–
MY-4	–	–	612	228	0.59	0.28	4.2	4.1
MY-6	–	–	595	274	0.66	0.36	5.8	6.0
MY-8	–	–	588	326	0.71	0.45	7.7	7.6
NiMo/HMY-0	3.8	10.8	348	126	0.32	0.14	–	–
NiMo/HMY-4	3.7	11.2	492	206	0.48	0.26	4.5	4.2
NiMo/HMY-6	3.8	11.2	504	268	0.54	0.32	6.1	5.9
NiMo/HMY-8	3.8	11.3	508	309	0.56	0.36	7.8	7.6

[a] Determined by ICP-OES.
[b] Calculated by the BET method.
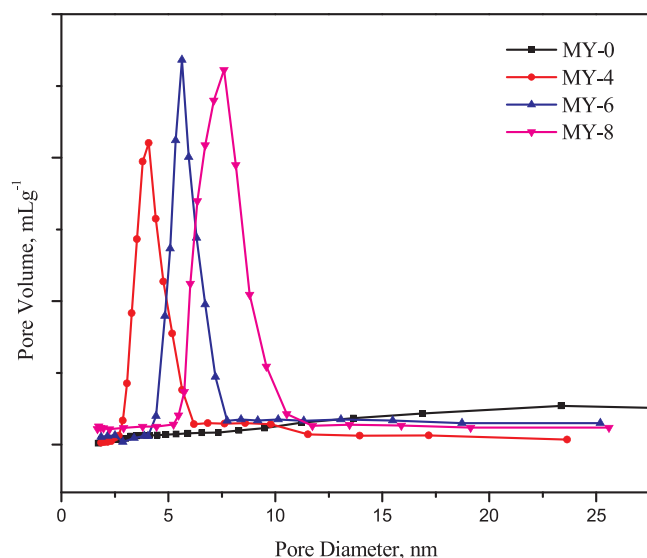[c] Obtained at a relative pressure of 0.99.

Fig. 2. Mesopore diameter distribution of the synthesized MY-x series zeolites.

with an increase in mesopore diameter consistent with results observed from SA XRD patterns.

To better understand changes in the textural properties of the MY-x series zeolites, a physisorption analysis of the prepared NiMo/HMY-x series catalysts was also performed, and the corresponding results are also summarized in Table 1. Table 1 shows total surface area and mesopore surface area values of catalyst NiMo/HMY-0 of 348 m^2 g^{-1} and 126 m^2 g^{-1}, respectively, and a total surface area for catalyst NiMo/HMY-0 that is approximately 280 m^2 g^{-1} lower than that of sample MY-0 due to the blocking of micropores after the incorporation of the active phase (NiMo); the mesopore surface area of catalyst NiMo/HMY-0 is approximately 50 m^2 g^{-1} higher than that of sample MY-0 due to the formation of mesopores during ion exchange process. After the incorporation of mesopores, the total surface area of catalyst NiMo/HMY-4 is only approximately 120 m^2 g^{-1} lower than that of sample MY-4, and the mesopore surface area remains nearly unchanged. With an increase in mesopore size, the total surface area only decreased by approximately 90 m^2 g^{-1} and 80 m^2 g^{-1} over catalysts NiMo/HMY-6 and NiMo/HMY-8 respectively, relative to MY-6 and MY-8. These results denote the presence of a pore confinement effect on MY-0 for the loading of active metals. The mesopore sizes of the NiMo/HMY-x series catalysts slightly increased relative to those of the MY-x series zeolites, which could be explained by the blockage of small mesopores following the incorporation of active metals.

NiO and MoO$_3$ levels deposited onto the NiMo/HMY-x series catalysts were determined from ICP-OES, and the corresponding results were summarized in Table 1. We clearly found that loadings of NiO over the NiMo/HMY-x series catalysts were similar, while the loadings of MoO$_3$ over the NiMo/HMY-x series catalysts increased in the following order: NiMo/HMY-0 (10.8 wt.%) < NiMo/HMY-4 (11.2 wt.%) = NiMo/HMY-6 (11.2 wt.%) ≈ NiMo/HMY-8 (11.3 wt.%). This suggests that the incorporation of broad and opened mesopores can enhance the loading and dispersion of active metals.

3.3. Acidity

Acidity properties of support materials often play very important roles in the loading of active metals and in the catalytic performance of the related supported bifunctional HDS catalysts, and they are determined by the compositions and structures of materials involved. The Py-FTIR spectra of the synthesized MY-x series samples are displayed in Fig. 3:

The IR vibration peak found at roughly 1543 cm^{-1} is assigned to
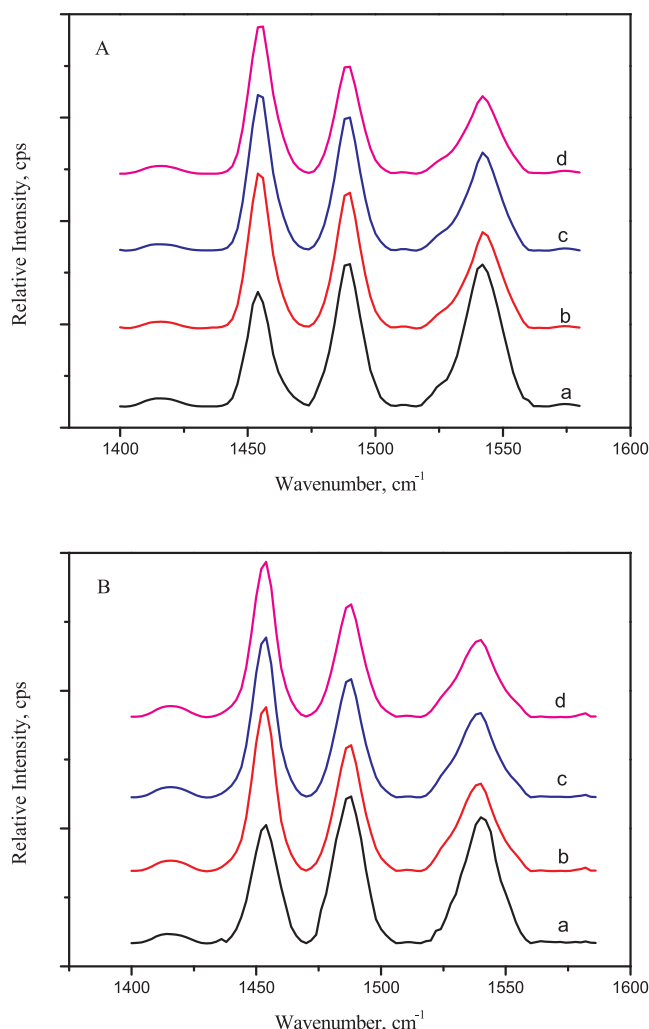

Fig. 3. Py-FTIR spectra of the HMY-x samples: (a) HMY-0, (b) HMY-4, (c) HMY-6 and (d) HMY-8; (A) after pyridine desorbed at 200 °C, (B) after pyridine desorbed at 350 °C.

pyridine ions adsorbed onto the Brönsted acid sites (BAS), and the IR vibration peak observed at approximately 1453 cm^{-1} is assigned to pyridine molecules combined with Lewis acid sites (LAS) according to the literatures [48,49]. More specifically, Fig. 3A displays the Py-FTIR profiles of the MY-x series samples after pyridine was desorbed at 200 °C, and Fig. 3B displays the Py-FTIR profiles of the MY-x series samples after pyridine was desorbed at 350 °C. The amounts of BAS and LAS were calculated according to the recorded Py-FTIR spectra (Fig. 3), and the corresponding results were summarized in Table 2. The results

Table 2
Amounts of Brönsted and Lewis acid sites determined by pyridine-FTIR of the HMY-x samples and the NiMo/HMY-x series catalysts.

Samples	200 °C, µmol g^{-1}			350 °C, µmol g^{-1}			Total
	LAS	BAS	BAS/LAS	LAS	BAS	BAS/LAS	
HMY-0	159	254	1.60	98	172	1.76	683
HMY-4	218	172	0.79	109	99	0.91	598
HMY-6	224	168	0.75	112	96	0.86	600
HMY-8	215	161	0.75	103	90	0.87	569
NiMo/HMY-0	248	302	1.22	196	245	1.25	991
NiMo/HMY-4	322	256	0.80	205	186	0.91	969
NiMo/HMY-6	335	248	0.74	212	184	0.87	979
NiMo/HMY-8	328	242	0.74	208	180	0.87	958

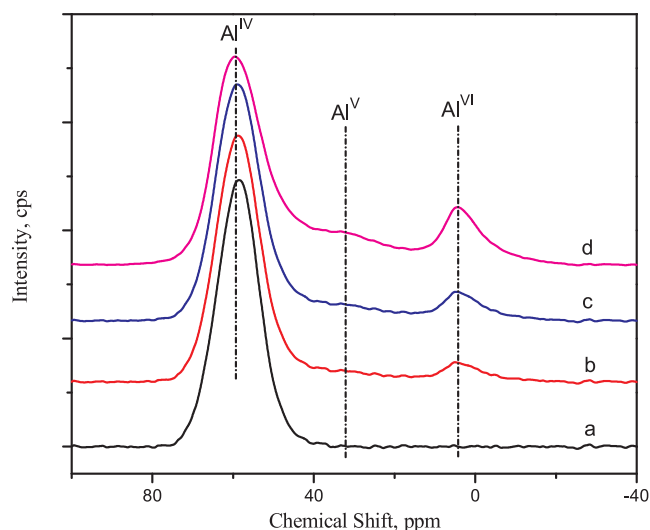**Fig. 4.** ^{27}Al MAS NMR spectra of the synthesized MY-x series zeolites: (a) MY-0, (b) MY-4, (c) MY-6 and (d) MY-8.
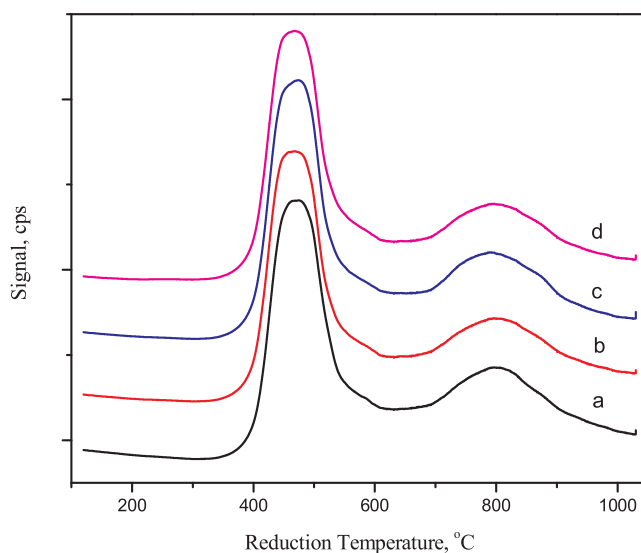

Fig. 5. H$_2$-TPR profiles of the synthesized NiMo/HMY-x series catalysts: (a) NiMo/HMY-0, (b) NiMo/HMY-4, (c) NiMo/HMY-6 and (d) NiMo/HMY-8.

clearly show that after mesopores were introduced into Y crystals, a significant change in the amounts of weak and strong acid sites was observed. Due to its relative high degree of crystallinity, HMY-0 presented more acid sites (683 μmol g^{-1}) than that of other samples; on the other hand, more BAS than LAS was found on the surfaces of sample HMY-0, and the BAS/LAS ratio reached as high as 1.60 (weak) and 1.76 (strong). After the incorporation of mesopores, the levels of both weak and strong LAS increased profoundly, while the levels of both weak and strong BAS decreased profoundly. The total amounts of acid sites in sample HMY-4 and HMY-6 also decreased to approximately 600 μμmol g^{-1}. All of these variations can be explained by a decrease in the crystallinity of mesopore walls and by a simultaneous increase in the amounts of non-framework Al species present in the mesopore walls as illustrated by the ^{27}Al MAS NMR profiles displayed in Fig. 4. Three signals with chemical shifts of approximately 60 ppm are assigned to tetrahedral Al (Al^{IV}) species, which are considered as the framework Al species. We assigned 32 ppm to five-coordination Al (Al^{V})species, which are considered the transition state Al species between framework Al species and non-framework Al species. Finally, we assigned 4 ppm to octahedral Al (Al^{VI}) species, which are considered non-framework Al species [44,50]. The intensity of the signal observed at approximately 60 ppm decreased in the following order: MY-0 > MY-4 > MY-6 > MY-8. Additionally, the intensity of the signal observed at approximately 4 ppm increased in the following order: MY-0 < MY-4 < MY-6 < MY-8. This suggests a decline occurring in the framework Al species and an increase in the non-framework Al species. Moreover, the signal assigned to Al^{V} species could only be detected when the mesopore diameter was greater than 6 nm. However, for sample HMY-8, the BAS/LAS ratio remained almost the same as that of sample HMY-6, but the amount of acid sites further decreased to that approximately 569 μmol g^{-1}, which can be explained by the formation of P zeolites (the WA XRD results displayed in Fig. 1) whose acidity levels are lower than those of Y zeolites.

BAS and LAS levels observed over the NiMo/HMY-x series catalysts were also detected from Py-FTIR, and the corresponding results are also summarized in Table 2:

Table 2 clearly shows that the levels of weak LAS observed over catalysts NiMo/HMY-4 (322 μmol g^{-1}) ≈ NiMo/HMY-6 (335 μmol g^{-1}) ≈ NiMo/HMY-8 (328 μmol g^{-1}) are obviously higher than those observed over catalyst NiMo/HMY-0 (248 μmol g^{-1}), while the amounts of strong LAS observed over the four investigated NiMo/HMY-x series catalysts are similar. The levels of weak BAS and strong BAS observed over catalysts NiMo/HMY-4 (256 μmol g^{-1}, 186 μmol g^{-1}) ≈

NiMo/HMY-6 (248 μmol g^{-1}, 184 μmol g^{-1}) ≈ NiMo/HMY-8 (242 μmol g^{-1}, 180 μmol g^{-1}) are obviously lower than those observed over catalyst NiMo/HMY-0 (302 μmol g^{-1}, 245 μmol g^{-1}). These results are basically consistent with those observed for the HMY-x series samples. Although the total amounts of acid sites observed over the HMY-x series catalysts are totally different to each other, the total amounts of acid sites over the investigated four catalysts are quite similar after the deposition of active metals, and the amounts of each type of acid site observed profoundly increased after the deposition of active metals.

3.4. H$_2$-TPR results

It is widely accepted that interactions between active metals and support (MSI) have important effects on the catalytic performance of the supported bifunctional HDS catalysts. H$_2$-TPR characterization is believed to be the most effective means of evaluating the MSI of a bifunctional HDS catalyst. The recorded H$_2$-TPR profiles of the NiMo/HMY-x series catalysts are displayed in Fig. 5. The results clearly reveal two individual H$_2$ consumption peaks centered at reduction temperatures of 430 °C and 800 °C that spur a reduction of Mo(VI) species to Mo (IV) species(the lower one) and a reduction of Mo(VI) to Mo. Futher, these Mo species strongly interact with supports (higher one) among the NiMo/HMY-x series catalysts [26]. The lower temperature H$_2$ consumption peak of the H$_2$-TPR profiles shifts slightly to an even lower temperature(with a temperature shift of less than 5 °C) after the incorporation of mesopores and potential due to variations in metal dispersion observed along the support surface. The higher temperature H$_2$ consumption peaks of catalysts NiMo/HMY-0 and NiMo/HMY-4 are almost the same, but for catalysts NiMo/HMY-6 and NiMo/HMY-8, they profoundly shift to a lower temperature (with a temperature shift of approximately 20 °C), revealing a weakened MSI between Mo species closely interacting with the support. The decrease in the MSI observed may be attributed to the higher sulfidation degree and catalytic performance of the corresponding catalysts [37].

3.5. HRTEM

For the bimetallic HDS catalysts, Ni promoted the MoS$_2$ structures, and namely, the NiMoS phases are considered to constitute the real active phase that supports the HDS reactions. Thus, the direct observation of Ni promoted MoS$_2$ structures and of dispersions of Ni-
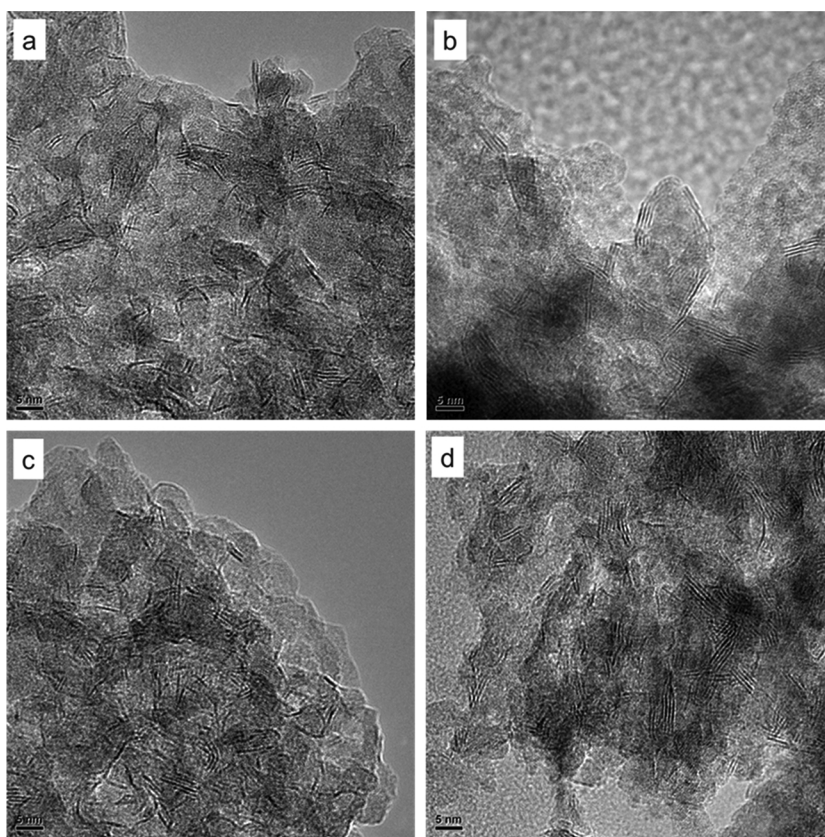
Fig. 6. HRTEM images of the sulfide NiMo/MY-x series catalysts: (a) NiMo/MY-0, (b) NiMo/MY-4, (c) NiMo/MY-6 and (d) NiMo/MY-8.

promoted MoS_2 slabs by HRTEM can help establish the relationship between mesopore sizes of supports and the morphology of Ni- promoted MoS_2 slabs, as the lattice fringes are visible at a different resolution [36]. This can help us establish the relationship between the morphology of Ni promoted MoS_2 slabs and catalytic performance in turn. Thus, HRTEM images of the newly created sulfide catalysts were taken, and the representative images of different catalysts are displayed in Fig. 6. The statistical results for stacking layer numbers distribution and slab length distributions of MoS_2 slabs based on no less than 400 catalysts were generated, and the representative images of different MoS_2 slabs are presented in Fig. 7. The statistical results based on our HRTEM results are summarized in Table 3:

HRTEM images of the NiMo/HMY-x series catalysts clearly present black two- dimensional thread-like fringes with an interlayer spacing of about 0.64 nm that is assigned to bulk MoS_2 slabs. It can be intuitively observed from the HRTEM images that the number of monolayer MoS_2 slabs present decreased profoundly after the introduction of mesopores into Y crystals, and it decreased further with an increase in mesopore diameter. The statistical stacking number distribution of the MoS_2 crystals over the investigated NiMo/HMY-x series catalysts displayed in Fig. 7A clearly illustrates that the dominant stacks of MoS_2 slabs over catalyst NiMo/HMY-0 include 1–2 layers and that after the introduction of mesopores into the support materials, dominant stacks of MoS_2 slabs over catalyst NiMo/HMY-4 increase to 2 layers. This then further increases to 3 layers over catalysts NiMo/HMY-6 and NiMo/HMY-8 with the increase of the mesopore diameter, thus the average stacking number of MoS_2 slabs of the corresponding sulfided catalysts increase in the same order: NiMo/HMY-0 (1.8) < NiMo/HMY-4 (2.4) < NiMo/HMY-6 (2.7) ≈ NiMo/HMY-8 (2.7), (Table 3). According to adsorption theory, the number of adsorption layers in heptamolybdate anions and Ni^{2+} ions along the surfaces of support is dependent on concentrations present in the impregnation solution and on the curvature of the support surface with higher concentrations and less curvature (lager pore

diameters) often leading to multilayer adsorption. In our case, the catalysts were prepared via the incipient impregnation method, to guarantee the same loading of both Ni and Mo species. The concentration of the impregnation solution decrease with an increase in mesopore diameter because the pore volume of the HMY-x samples increased with mesopore diameter (Table 1), leading to a decline in the adsorption layer of Ni and Mo precursors. On the other hand, an increase in mesopore diameter denotes a decline in surface curvature, which facilitates multilayer adsorption and which leads to an expansion of the adsorption layer in Ni and Mo precursors. Therefore, samples NiMo/HMY-6 and NiMo/HMY-8 present similarly larger adsorption layers of both Ni and Mo precursors. The larger adsorption layer of the Mo precursor implies presence of a thicker MoO_3 after calcination, leading to a decrease in the polarization effects of Al^{3+} species and in oxygen effect, and further spurring an increase in the stacking number of MoS_2 crystals after they were sulfided. The statistical results summarized in Table 3 illustrate that the average slab length of MoS_2 slabs did not change considerably, especially for catalysts NiMo/HMY-4 (5.0 nm), NiMo/HMY-6 (4.8 nm) and NiMo/HMY-8 (4.7 nm). However, the statistical slab length distribution of the MoS_2 crystals over the investigated NiMo/HMY-x series catalysts displayed in Fig. 7B clearly presents variations in MoS_2 slabs lengths between catalysts: the dominant slab length for MoS_2 slabs over catalyst NiMo/HMY-0 is 5–7 nm, while it becomes 4–6 nm after the introduction of mesopores into support materials. For catalysts NiMo/HMY-6 and NiMo/HMY-8, the dominant slab length of MoS_2 crystals further decreases to 4–5 nm because more Ni atoms were doped into the MoS_2 slabs(proven by the XPS results), decreasing the periodicity of the Mo species and shortening the slab length of MoS_2 slabs. Proportions of Mo atoms located along both edge sites and corner sites of the MoS_2 crystals were calculated according to the statistical results and are also summarized in Table 3. The results show that the dispersion of Mo species (D_{Mo}), the proportion of Mo species located along edge sites of MoS_2 crystals (f_{Moe}) and the
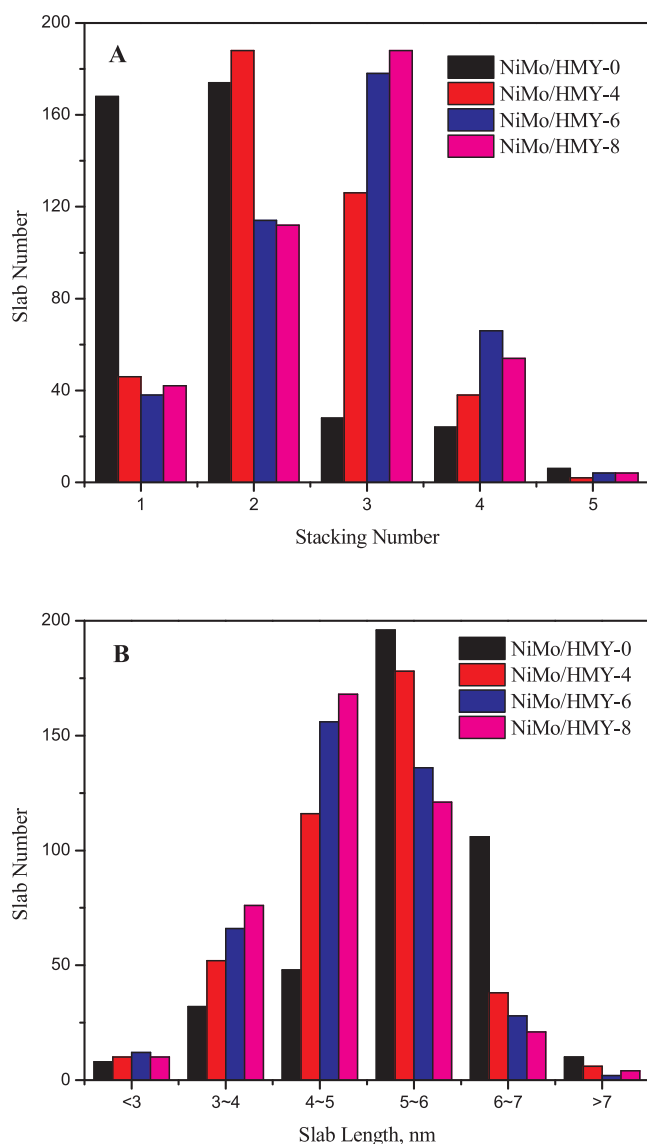
Fig. 7. The statistical stacking number distribution(A) and the slab length distribution(B) of the MoS$_2$ crystals over NiMo/HMY-x series catalysts.

Table 3
The statistical result for MoS$_2$ slabs of the NiMo/HMY-x series catalysts.

Catalysts	Average length (nm)	Average stacking number	D_{Mo}	f_{Moe}	f_{Moc}	f_{Moe}/f_{Moc}
NiMo/HMY-0	5.5	1.8	0.21	0.18	0.026	7.09
NiMo/HMY-4	5.0	2.4	0.24	0.21	0.032	6.61
NiMo/HMY-6	4.8	2.7	0.26	0.22	0.037	6.00
NiMo/HMY-8	4.7	2.7	0.26	0.22	0.038	5.84

proportion of Mo species located at corner sites of MoS$_2$ crystals (f_{Moc}) increased in the following order: NiMo/HMY-0 (0.21, 0.18, 0.026) < NiMo/HMY-4 (0.24, 0.21, 0.032) < NiMo/HMY-0 (0.26, 0.22, 0.037) ≈ NiMo/HMY-4 (0.26, 0.22, 0.038). This again indicates that the mesopore size of support materials plays an important role in the morphology of active phases of corresponding HDS catalysts.

3.6. XPS results

The covalent states and sulfidation degrees of Mo and Ni species over the sulfided NiMo/HMY-x series catalysts were investigated by XPS. Fig. 8 displays the Mo 3d XPS spectra and corresponding deconvolution results for the investigated NiMo/HMY-x series catalysts. The Ni 2p XPS spectra and deconvolution results for the investigated NiMo/HMY-x series catalysts are displayed in Fig. 9:

To further understand the effects of mesopore diameters on the sulfidation of Ni and Mo species, we present deconvolution data in Table 4. The deconvolution of Mo 3d- level XPS spectra occured as follows: the peak with a binding energy level of approximately 226.6 eV is ascribed to S^{2-} species; peaks with binding energy levels of roughly 228.9 ± 0.2 eV and 231.7 ± 0.2 eV are ascribed to the Mo 3d$_{5/2}$ and Mo 3d$_{3/2}$ levels for Mo^{4+} species, respectively; peaks with binding energy levels of roughly 230.5 ± 0.2 eV and 233.6 ± 0.2 eV are ascribed to the Mo 3d$_{5/2}$ and Mo 3d$_{3/2}$ levels for Mo^{5+} species, respectively; and peaks with binding energy levels of roughly 232.7 ± 0.2 eV and 236.0 ± 0.2 eV are respectively ascribed to the Mo 3d$_{5/2}$ and Mo 3d$_{3/2}$ levels for Mo^{6+} species according to the reported results [15,29,51]. As is clearly shown in Table 4, the sulfidation of Mo species (Mo^{4+} proportion) was enhanced in the following order: NiMo/HMY-0 (60.4%) < < NiMo/HMY-4 (70.6%) < NiMo/HMY-6 (73.3%) ≈ NiMo/HMY-8 (73.1%). We can thus conclude that widely opened mesopores favor the sulfidation of Mo species. According to the theory proposed above, an increase in the thickness of MoO$_3$ precursors results in a decline in polarization effects of Al^{3+} species and in the oxygen effect, spurring a decline in the MSI of the corresponding catalyst and enhancing the sulfidation of Mo species. As Mo atoms located along edge sites and corner sites are considered to be real active sites [46,52], it is believed that hydrogenation reactions mainly take place along the edges of MoS$_2$ slabs, while DDS reactions are more likely to take place in the corner sites of MoS$_2$ crystals [47,53]. Thus, the proportions of Mo atoms located along the edge(Moe) and at the corner(Moc) sites were calculated according to the HRTEM and Mo 3d XPS results using the following equations:

$$Moe = MoS_2 * f_{Moe} \qquad (7)$$

$$Moc = MoS_2 * f_{Moc} \qquad (8)$$

where MoS$_2$ is the proportion of MoS$_2$ over each catalyst in % obtained from the XPS deconvolution results; the results are also summarized in Table 4. It is clearly that Moe and Moc values of the investigated catalysts increased in the same order: NiMo/HMY-0 (10.9%, 1.57%) < NiMo/HMY-4 (14.8%, 2.26%) < NiMo/HMY-6 (16.1%, 2.71%) ≈ NiMo/HMY-8 (16.1%, 2.78%). Indicating that the widely opened mesopores favors the formation of active edge sites and active corner sites.

The deconvolution data for Ni 2p XPS spectra are as follows: the deconvolution peak with a binding energy level of 853.5 ± 0.5 eV is ascribed to the NiS$_x$ species, the peak with a binding energy level of 855.5 ± 0.5 eV is ascribed to the NiMoS phase and the peak with a binding energy level of 857.3 ± 0.5 eV is ascribed to the Ni^{2+} species [54]. Both the sulfidation degree of the Mo species, which is defined as Mo^{4+}/Mo$_{total}$, and the sulfidation degree of the Ni species(Ni$_{sul}$), which is defined as (NiS$_x$ + NiMoS)/Ni$_{total}$, were calculated according to deconvolution results, and the corresponding date are summarized in Table 4. The results clearly show that all of the investigated NiMo/HMY-x series catalysts exhibit relatively high levels of sulfidation for Ni species (with an Ni$_{sul}$ of greater than 90%) and that sulfidation levels and proportions of NiMoS phase slightly increase after the introduction of mesopores into the support materials, increasing further with an increase in mesopore diameter. It is widely accepted that all Ni atoms doped into MoS$_2$ crystals are located on the edge sites or corner sites of MoS$_2$ crystals rather than in bulky MoS$_2$ crystals [55,56], which would favor the formation of more active "Type II NiMoS" phases over the corresponding HDS catalysts.
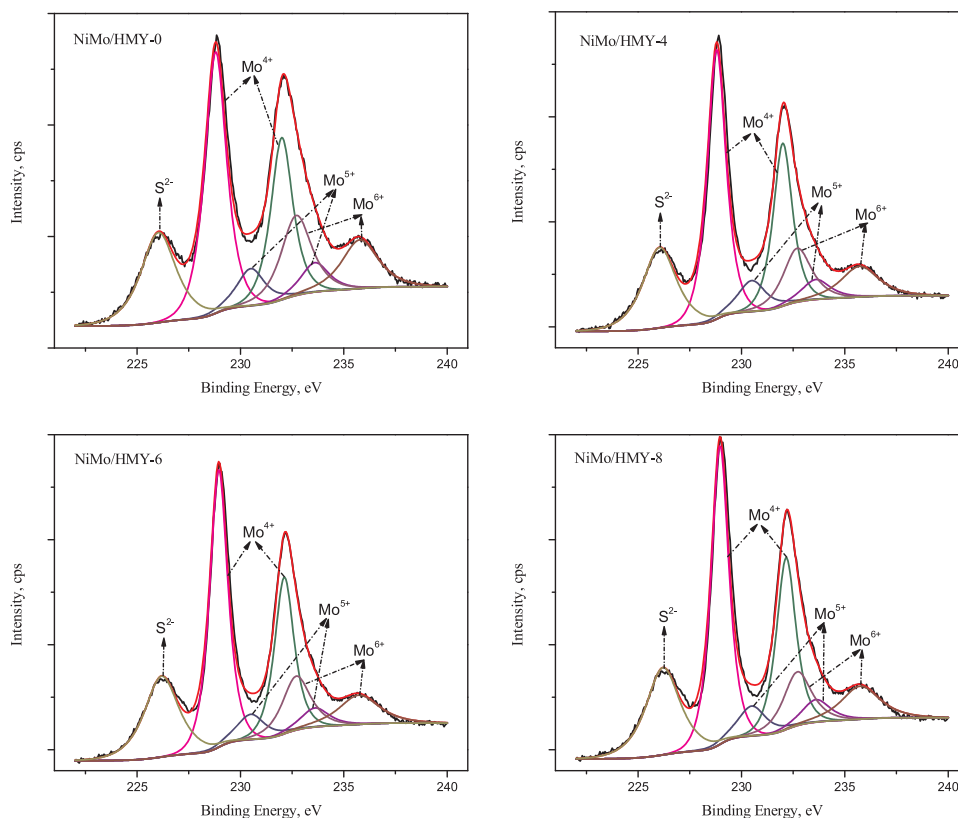
Fig. 8. Deconvolution results of Mo 3d XPS spectra of the sulfided NiMo/MY-x series catalysts.
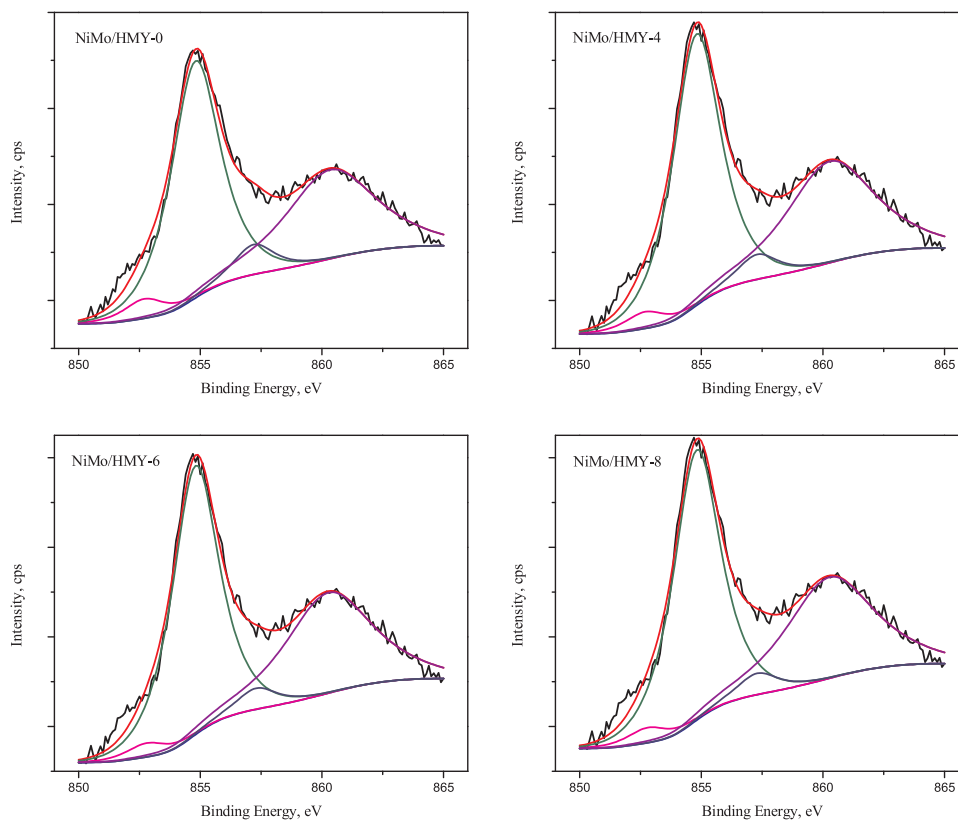

Fig. 9. Deconvolution results of Ni 2p XPS spectra of the sulfided NiMo/MY-x series catalysts.

Table 4
XPS deconvolution results of the sulfide NiMo/HMY-x series catalysts.

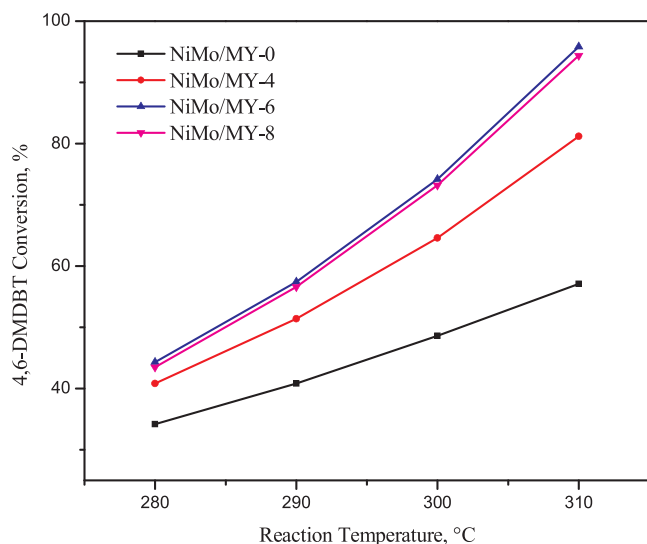| Catalysts Proportion, (%)	MoS$_2$	MoO$_x$S$_y$	MoO$_3$	Ni$_{sul}$	NiO	NiS$_x$	NiMoS	Moe	Moc
NiMo/HMY-0	60.4	12.2	27.4	91.0	9.0	5.9	85.1	10.9	1.57
NiMo/HMY-4	70.6	9.8	19.6	93.0	7.0	4.7	88.4	14.8	2.26
NiMo/HMY-6	73.3	8.4	18.3	93.9	6.1	4.0	89.8	16.3	2.71
NiMo/HMY-8	73.1	9.2	17.7	93.9	6.1	4.4	89.5	16.2	2.78

Fig. 10. Conversion of 4,6-DMDBT over the sulfided NiMo/MY-x series catalysts at different reaction temperatures.

3.7. Catalytic performance

The catalytic performance of the prepared NiMo/HMY-x series catalysts was evaluated by using 4,6-DMDBT as a probe molecule on a fixed bed reactor with total pressure level of 5 MPa and by using WHSV of 40 h^{-1} at different reaction temperatures (in the range of 280~310 °C), The products generated were carefully collected and analyzed offline using an Agilent 4890D gas chromatograph. Conversions of 4,6-DMDBT measured at different reaction temperatures over different catalysts are displayed in Fig. 10.

The results clearly show that 4,6-DMDBT conversions made for the investigated NiMo/HMY-x series catalysts increased in the following order at all of the investigated reaction temperatures: NiMo/HMY-0 < < NiMo/HMY-4 < NiMo/HMY-8 ≈ NiMo/HMY-6. This implies that the catalytic activity of the NiMo/HMY-x series catalysts increased in the same order. Therefore, catalyst NiMo/HMY-6 exhibits superior catalytic performance amidst 4,6-DMDBT HDS reactions at all of the investigated reaction temperatures. To draw a more detailed comparison, the activation energies of the global HDS reaction occurring over different catalysts at a reaction temperature of 290 °C were calculated according to the following equation:

$$E_a = \frac{RT}{(T_1 - T_2)} \ln \frac{x_1}{x_2} \tag{9}$$

where E_a is the activation energy, T = 563.15 K, T_1 and T_2 are the reaction temperatures in K, and x_1 and x_2 are the conversions of 4,6-DMDBT at reaction temperatures of T_1 or T_2, respectively. The corresponding informations are summarized in Table 5:

The results show that activation energies of the investigated catalysts increased in the following order: NiMo/HMY-0 (81.5 kJ mol^{-1}) < NiMo/HMY-4 (108.0 kJ mol^{-1}) < NiMo/HMY-6 (121.2 kJ mol^{-1}) ≈ NiMo/HMY-8 (121.8 kJ mol^{-1}). The global activation energies of 4,6-DMDBT HDS over catalysts NiMo/HMY-6 and NiMo/

Table 5
Activation energies and rate constants of 4,6-DMDBT HDS reactions over NiMo/HMY-x series catalysts at 290 °C(with 4,6-DMDBT conversion of 50 ± 0.4%).

Catalysts	Ea (kJ mol^{-1})	TOF (h^{-1})	k$_{HDS}$	k$_{DDS}$	k$_{HYD}$	K$_{ISO}$	HYD/DDS[a]
			μmol h^{-1} g^{-1}				
NiMo/HMY-0	81.5	1.8	307	138	98	178	0.71 (1.47)
NiMo/HMY-4	108.0	2.9	617	259	173	426	0.63 (2.44)
NiMo/HMY-6	121.2	3.5	783	337	196	572	0.58 (2.86)
NiMo/HMY-8	121.8	3.4	761	327	190	571	0.58 (3.18)

[a] The values in the brackets are the ratios of HYD/DDS that not count those isomerized products.

HMY-8 are comparable to those reported in the literatures [14,21,28,30,49], while the global activation energies of 4,6-DMDBT HDS over catalysts NiMo/HMY-0 and NiMo/HMY-4 are clearly lower than those reported results. This suggests the existence of a pore confinement effect (diffusion limitation) for 4,6-DMDBT on these two catalysts, which will be further proven through the calculation of reaction rate constants and turnover frequencies.

Fig. 11 displays 4,6-DMDBT conversions over the investigated NiMo/HMY-x series catalysts with different WHSVs for a reaction temperature of 290 °C. Clearly, 4,6-DMDBT conversions increased with a decline in WHSVs for each catalyst, and 4,6-DMDBT conversions for catalysts NiMo/HMY-6 and NiMo/HMY-8 are similar for all of the investigated WHSVs. These values are higher than those for catalysts NiMo/HMY-4 and NiMo/HMY-0. This shows that the pore diffusion limitations of 4,6-DMDBT were completely eliminated for catalyst NiMo/HMY-6. To further compare the catalytic performance of the investigated NiMo/HMY-x series catalysts, product distributions of 4,6-DMDBT HDS for the investigated NiMo/HMY-x series catalysts with a 4,6-DMDBT conversion of 50 ± 0.4% (executed by changing WHSVs) were analyzed off-line by means of GC-MS, and the corresponding results are summarized in Table 6. The global rate constant for 4,6-DMDBT HDS reaction was calculated according to the following equation employing the pseudo first-order reaction model:

$$kHDS = \frac{F}{m} \ln\left(\frac{1}{1-x}\right) = \frac{W \cdot \omega \cdot \ln\left(\frac{1}{1-x}\right)}{M} \tag{10}$$
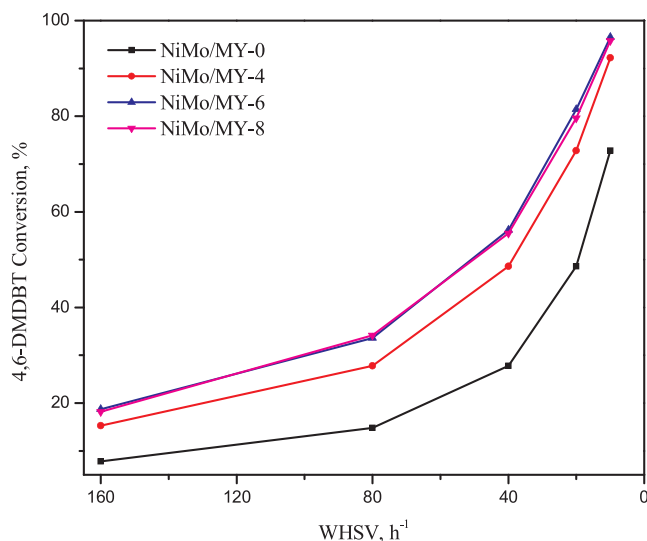

Fig. 11. Conversion of 4,6-DMDBT over the sulfided NiMo/MY-x series catalysts at different WHSVs. (290 °C).

Table 6
Products distributions of different catalysts for 4,6-DMDBT HDS.

Catalysts	Products selectivity, (%)					
	HYD		DDS	ISO		
	T(H)HDMDBT	3,3'-DMCHB + 3,3'-DMBCH	3,3'-DMBP	3,4'- and 4,4'-DMBP	3,6- and 3,7-DMDBT	Iso-MIPTs
NiMo/HMY-0	9	16	17	28	23	7
NiMo/HMY-4	8	14	9	33	30	6
NiMo/HMY-6	8	12	7	36	32	5
NiMo/HMY-8	7	12	6	37	32	6

[a]All the product distributions were analyzed with 4,6-DMDBT conversion of 50 ± 0.4% by changing the WHSVs (290 °C, 4 MPa, 200 mL/mL).

where F is the feeding rate of 4,6-DMDBT in mol h^{-1}, m is the mass of the loaded catalyst in g, x is the conversion of 4,6-DMDBT, W is the WHSV, ω is the mass concentration of 4,6-DMDBT in the feed and M is the molar mass of 4,6-DMDBT. The turnover frequencies (TOF) of 4,6-DMDBT over different catalysts were also calculated according to the following equation [57,58]:

$$TOF = (F \cdot x)/(n_{Mo} \cdot D_{Mo}) \qquad (11)$$

The corresponding results are also summarized in Table 5. The results clearly show that TOF values for the investigated NiMo/HMY-x series catalyst increased in the following order: NiMo/HMY-0 (1.8 h^{-1}) < < NiMo/HMY-4 (2.9 h^{-1}) < NiMo/HMY-8 (3.4 h^{-1}) ≈ NiMo/HMY-6 (3.5 h^{-1}). As most physicochemical properties except for mesopore sizes of the HMY-0 series supports are similar, different TOF values observed among the investigated catalysts can be attributed to the presence of pore confinement effects on catalysts NiMo/HMY-0 and NiMo/HMY-4. The rate constants of the DDS pathway (k_{DDS}), HYD pathway (k_{HYD}) and ISO pathway (k_{ISO}) were also calculated based on global rate constants and product distributions according to the following equations:

$$k_{DDS} = k_{HDS} \cdot S_{DDS} \qquad (12)$$

$$k_{HYD} = k_{HDS} \cdot S_{HYD} \qquad (13)$$

$$k_{ISO} = k_{HDS} \cdot S_{ISO} \qquad (14)$$

where S_{DDS} is the proportions (Table 6) of DMBPs in the HDS products; S_{HYD} is the sum of the proportions (Table 6) for T(H)HDMDBT, DMCHB, DMBCH and Iso-MIPTs in the HDS products; and S_{ISO} is the sum of the proportions (Table 6) of 3,4'-DMBP, 4,4'-DMBP, 3,6-DMDBT, 3,7-DMDBT and Iso-MIPTs in the HDS products. These results are also summarized in Table 5. It is clear that global rate constants of 4,6-DMDBT HDS for the investigated NiMo/HMY-x series catalysts can be organized in the following order: NiMo/HMY-0 (307 μmol h^{-1}g^{-1}) < <

NiMo/HMY-4 (617 μmol h^{-1}g^{-1}) < NiMo/HMY-8 (761 μmol h^{-1}g^{-1}) ≈ NiMo/HMY-6 (783 μmol h^{-1}g^{-1}). This can be explained by the theory that the Mo atoms located at the coordination unsaturated sites(CUS) of MoS$_2$ slabs are the real active sites for 4,6-DMDBT HDS reactions, these CUS Mo atoms can adsorb and activate 4,6-DMDBT molecules. After the incorporation of Ni species into MoS$_2$ slabs, more CUS sites would be formed, and thus the catalytic performance of the corresponding catalysts greatly improved. On the other hand, Ni species can adsorb and activate the H2 molecules more easily than Mo species. Thus, with more Ni atoms embedded into MoS$_2$ species, the catalytic centers for H$_2$ activation are closer to those catalytic centers for 4,6-DMDBT activation, results in an even higher catalytic performance [59]. As noted above, Mo atoms located along both edge and corner sites are the real active sites of 4,6-DMDBT HDS, and the HRTEM (D$_{Mo}$, Table 3) and XPS results show that both the sulfidation degree of Mo species and the D$_{Mo}$ value increased in the following order: NiMo/HMY-0 < NiMo/HMY-4 < NiMo/HMY-6 ≈ NiMo/HMY-8. This shows that the number of active edge and corner sites increased

in the same order and thus that the catalytic performance of the investigated catalysts was enhanced in the above order. The k$_{DDS}$ of 4,6-DMDBT HDS for catalyst NiMo/HMY-6 is about 2.5 times the value found for catalyst NiMo/HMY-0, while the k$_{HYD}$ of 4,6-DMDBT HDS found for catalyst NiMo/HMY-6 is only approximately 2 times that found for catalyst NiMo/HMY-0, indicating that the introduction of mesopores into the catalyst support can affect HDS pathway selectivity. This is the case because methyl groups on the 4- and 6-positions strictly restrict 4,6-DMDBT molecules adsorbed onto the active corner sites through σ-adsorption. This is considered to be related to the DDS pathway of 4,6-DMDBT [60]. After the introduction of widely opened mesopores, more 4,6-DMDBT molecules can diffuse to acid sites located in the super cages of Y zeolites [36], and then they can be isomerized into 3,6- and 3,7-DMDBT, which have less pronounced substitution effects. Therefore, the σ-adsorption of isomerized molecules occurs more easily than it does for 4,6-DMDBT molecules. In turn, DDS activity and DDS pathway selectivity are enhanced. This can also be proven by the fact that the k$_{ISO}$ of 4,6-DMDBT HDS for catalyst NiMo/HMY-6 is approximately 3.2 times that for catalyst NiMo/HMY-0. According to product distributions and kinetic studies, a reaction network for 4,6-DMDBT HDS reaction is given in Fig. 12. 4,6-DMDBT can be transferred through three completely different pathways involving NiMo/HMY-x series catalysts: the sulfur heteroatom can be removed directly to produce 3,3'-DMBP, which is defined as the DDS pathway; 4,6-DMDBT molecules first undergo hydrogenation to produce T(H)HDMDBT as an intermediate that undergoes desulfurization. This pathway is defined as the HYD pathway. Additionally, 4,6-DMDBT molecules first undergo isomerization to produce 3,6- or 3,7-DMDBTvia the ISO pathway. Through this pathway, desulfurization of 3,6- or 3,7-DMDBT occurs via the DDS pathway or HYD pathway. The correlation between the HYD/DDS ratio and f$_{Moe}$/f$_{Moc}$ is displayed in Fig. S4, and the correlation between the HYD/DDS ratio and Moe/Moc is displayed in Fig. S5. The results show that the HYD/DDS ratio of the investigated catalysts is consistant with the f$_{Moe}$/f$_{Moc}$ and Moe/Moc, which are highly consistent with the reported results [44,61]. However, the HYD/DDS ratio is linearly dependent on neither the f$_{Moe}$/f$_{Moc}$ nor the Moe/Moc. This is the case because, on the one hand, the investigated NiMo/HMY-x series catalysts exhibit different levels of isomerization activity for 4,6-DMDBT, while isomerized intermediates exhibit different HYD/DDS ratios from those of 4,6-DMDBT. On the other hand, the introduction of widely opened mesopores mitigates steric hindrances caused by the presence of substituted methyl groups, and this enhances the accessibility of reactant molecules to active sites. Therefore, the HYD/DDS ratio of 4,6-DMDBT found for the investigated NiMo/HMY-x series catalysts is not only dependent on f$_{Moe}$/f$_{Moc}$ or Moe/Moc, but also on mesopore diameter and on the isomerization capacities of catalysts.

It is widely accepted that the morphologies of active phases play important roles in the selectivity of different HDS reaction pathways, and numerous studies have discussed the correlations between the selectivity of different HDS pathways and the

dispersion of Mo atoms within MoS$_2$ slabs, the promoter effect, the adsorption state of organosulfides and even the f$_{Moe}$/f$_{Moc}$ values
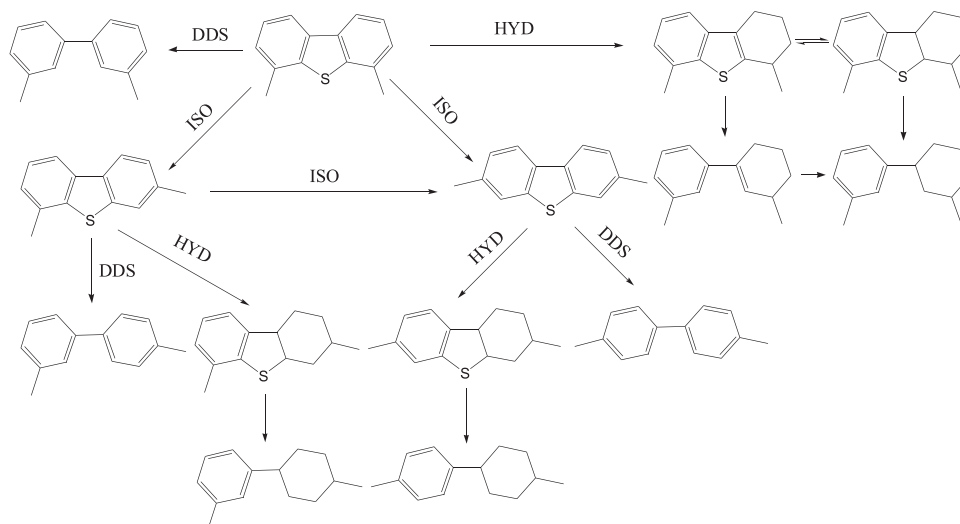
Fig. 12. The reaction network for 4,6-DMDBT HDS over the NiMo/HMY-x series catalysts.
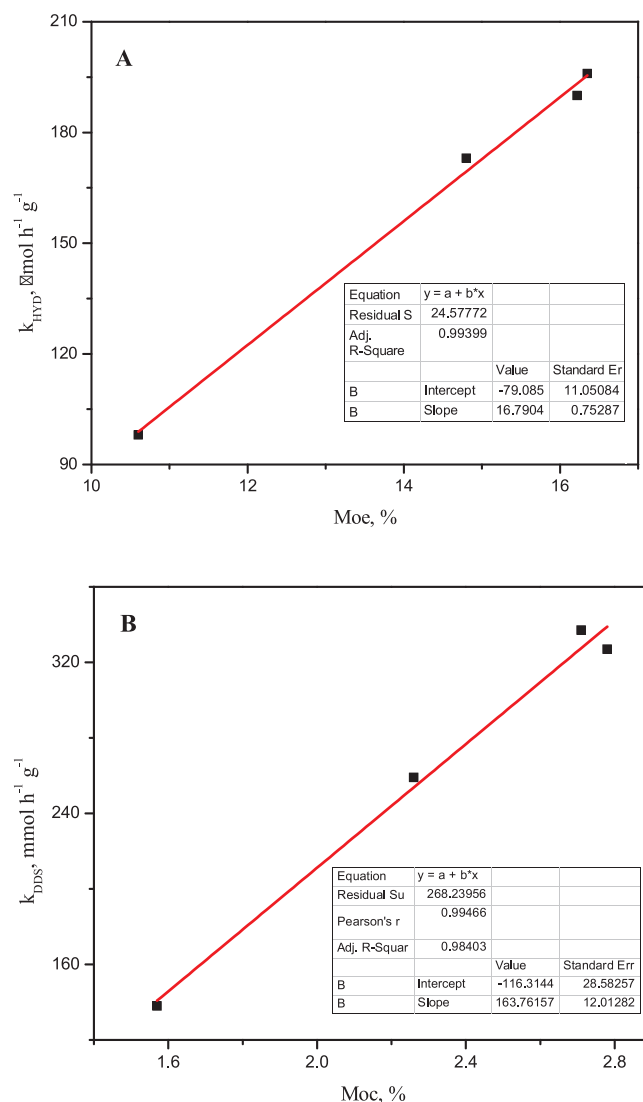

Fig. 13. The correlation between Moe and k_{HYD}(A) and the correlation between Moc and k_{DDS}(B) at the reaction temperature of 290 °C.

[6,7,60,62,63]. It has been confirmed that the addition of promoters shortens the slab length of MoS_2 crystals and enhances the dispersion of Mo species, facilitating the formation of corner active sites at which 4,6-DMDBT molecules prefer to adsorb via σ-adsorption. It has also been confirmed that 4,6-DMDBT molecules prefer to adsorb at active edge sites via π-adsorption, that 4,6-DMDBT molecules adsorbed via σ-adsorption are further transformed through the DDS pathway and that 4,6-DMDBT molecules adsorbed via π-adsorption are further transformed through the HYD pathway [60]. As the DDS pathway is related to active corner sites, while the HYD pathway is related to active edge sites, both the relationship between Moe and the rate constant of the HYD pathway and the relationship between Moc and the rate constant of the DDS pathway were investigated in this study, and the corresponding results are displayed in Fig. 13. It is clearly shown that the rate constant of the HYD pathway is linearly correlated with Moe, while the rate constant of the DDS pathway is linearly correlated with Moc. This is the case because Moe denotes the proportion of Mo atoms located along edge sites of MoS_2 slabs to the total number of Mo atoms supported on corresponding catalysts, while Moc denotes the proportion of Mo atoms located at corner sites of MoS_2 slabs to the total number of Mo atoms supported on investigated catalysts. Additionally, the Mo loadings of the investigated catalysts are identical, showing that the same number of Mo atoms is present on the investigated catalysts. We thus conclude that the rate constant of the HYD pathway is linearly correlated with Mo atoms located at the edge sites of MoS_2 crystals, while the DDS pathway is linearly correlated with Mo atoms located at the corner sites of MoS_2 slabs. Moreover, the slope of k_{DDS} to Moc (163.8) is roughly ten times that of k_{HYD} to Moe (16.8), indicating that the active corner sites are approximately ten times more active than the active edge sites.

4. Conclusion

NiMo supported on meso-microporous Y zeolites with similar physicochemical properties but with different mesopore sizes was synthesized, and we studied the properties of corresponding catalysts and of the 4,6-DMDBT HDS of the investigated catalysts. A reaction network of 4,6-DMDBT HDS for NiMo/HMY-x series catalysts was proposed. The mesopore size of the support plays an important role in the adsorption layer of Mo precursors, leading to the generation of MoO_3 of varying thickness. Larger mesopores inhibit the polarization effects of Al^{3+} and decrease MSI values of the corresponding catalyst, enhancing the sulfidation of Ni and Mo species, increasing stacking level, decreasing the slab length of MoS_2 slabs, and generating different proportions between

the active edge and corner sites. Micropores and mesopores with diameters of less than 4 nm have pore confinement effects on the HDS of 4,6-DMDBT, and steric hindrance caused by methyl groups of the 4- and 6- positions is diminished when mesopore diameters reache 6 nm. Widely opened mesopores favor the formation of active edge and corner sites, and thus, NiMo/HMY-6 catalyst exhibits superior catalytic performance for 4,6-DMDBT HDS. The HYD activity of NiMo/HMY series catalysts is linearly correlated to the number of Mo atoms located along edge sites of MoS_2 slabs, and the DDS activity of NiMo/HMY series catalysts is linearly correlated to the number of Mo atoms located at the corner sites of MoS_2 slabs. Moreover, active corner sites are approximately 10 times more active than active edge sites.

Acknowledgment

Appendix A. Supplementary data

Supplementary material related to this article can be found, in the online version, at doi:https://doi.org/10.1016/j.apcatb.2018.07.042.

References

[1] S. Rangarajan, M. Mavrikakis, ACS Catal. 7 (2016) 501–509.
[2] W. Fu, L. Zhang, T. Tang, Q. Ke, S. Wang, J. Hu, G. Fang, J. Li, F.S. Xiao, J. Am. Chem. Soc. 133 (2011) 15346–15349.
[3] M. Egorova, R. Prins, J. Catal. 224 (2004) 278–287.
[4] R. Singh, D. Kunzru, S. Sivakumar, Appl. Catal., B 185 (2016) 163–173.
[5] T. Tang, L. Zhang, W. Fu, Y. Ma, J. Xu, J. Jiang, G. Fang, F.S. Xiao, J. Am. Chem. Soc. 135 (2013) 11437–11440.
[6] X. Tao, Y. Zhou, Q. Wei, G. Yu, Q. Cui, J. Liu, T. Liu, Fuel Process. Technol. 118 (2014) 200–207.
[7] L. van Haandel, M. Bremmer, P.J. Kooyman, J.A.R. van Veen, T. Weber, E.J.M. Hensen, ACS Catal. 5 (2015) 7276–7287.
[8] Z. Vít, D. Gulková, L. Kaluža, J. Kupčík, Appl. Catal., B 179 (2015) 44–53.
[9] X. Li, Y. Chai, B. Liu, H. Liu, J. Li, R. Zhao, C. Liu, Industrial & Engineering Chemistry Research 53 (2014) 9665–9673.
[10] A. López-Benítez, G. Berhault, A. Guevara-Lara, Appl. Catal., B 213 (2017) 28–41.
[11] J. Xu, T. Huang, Y. Fan, Appl. Catal., B 203 (2017) 839–850.
[12] T. Zepeda, B. Pawelec, J. Fierro, T. Halachev, Appl. Catal., B 71 (2007) 223–236.
[13] A. López-Benítez, G. Berhault, A. Guevara-Lara, J. Catal. 344 (2016) 59–76.
[14] J. Jiao, J. Fu, Y. Wei, Z. Zhao, A. Duan, C. Xu, J. Li, H. Song, P. Zheng, X. Wang, Y. Yang, Y. Liu, J. Catal. 356 (2017) 269–282.
[15] R. Huirache-Acuña, T.A. Zepeda, E.M. Rivera-Muñoz, R. Nava, C.V. Loricera, B. Pawelec, Fuel Lond. (Lond) 149 (2015) 149–161.
[16] O.Y. Gutiérrez, T. Klimova, J. Catal. 281 (2011) 50–62.
[17] M. Gousi, C. Andriopoulou, K. Bourikas, S. Ladas, M. Sotiriou, C. Kordulis, A. Lycourghiotis, Appl. Catal., A 536 (2017) 45–56.
[18] A. Guevara-Lara, A.E. Cruz-Pérez, Z. Contreras-Valdez, J. Mogica-Betancourt, A. Alvarez-Hernández, M. Vrinat, Catal. Today 149 (2010) 288–294.
[19] M. Egorova, J. Catal. 225 (2004) 417–427.
[20] H. Wang, R. Prins, J. Catal. 264 (2009) 31–43.
[21] G. Pérot, Catal. Today 86 (2003) 111–128.
[22] Y.-K. Lee, Y. Shu, S.T. Oyama, Appl. Catal., A 322 (2007) 191–204.
[23] S. Mohanty, K. Chandra Mouli, K. Soni, J. Adjaye, A.K. Dalai, Appl. Catal., A 419-420 (2012) 1–12.
[24] L. Zhang, W. Fu, Q. Ke, S. Zhang, H. Jin, J. Hu, S. Wang, T.-d. Tang, Appl. Catal., A 433-434 (2012) 251–257.
[25] A. Duan, T. Li, Z. Zhao, B. Liu, X. Zhou, G. Jiang, J. Liu, Y. Wei, H. Pan, Appl. Catal., B 165 (2015) 763–773.
[26] F.J. Méndez, O.E. Franco-López, X. Bokhimi, D.A. Solís-Casados, L. Escobar-Alarcón, T.E. Klimova, Appl. Catal., B 219 (2017) 479–491.
[27] G. Wan, A. Duan, Y. Zhang, Z. Zhao, G. Jiang, D. Zhang, Z. Gao, Catal. Today 149 (2010) 69–75.
[28] W. Zhou, Y. Zhou, Q. Wei, L. Du, S. Ding, S. Jiang, Y. Zhang, Q. Zhang, Chemistry (Easton) 23 (2017) 9369–9382.
[29] W. Zhou, M. Liu, Y. Zhou, Q. Wei, Q. Zhang, S. Ding, Y. Zhang, T. Yu, Q. You, Energy Fuels 31 (2017) 7445–7455.
[30] H. Wu, A. Duan, Z. Zhao, D. Qi, J. Li, B. Liu, G. Jiang, J. Liu, Y. Wei, X. Zhang, Fuel Lond. (Lond) 130 (2014) 203–210.
[31] Y.V. Vatutina, O.V. Klimov, K.A. Nadeina, I.G. Danilova, E.Y. Gerasimov, I.P. Prosvirin, A.S. Noskov, Appl. Catal., B 199 (2016) 23–32.
[32] D. Verboekend, G. Vilé, J. Pérez-Ramírez, Adv. Funct. Mater. 22 (2012) 916–928.
[33] F.N. Gu, F. Wei, J.Y. Yang, N. Lin, W.G. Lin, Y. Wang, J.H. Zhu, Chem. Mater. 22 (2010) 2442–2450.
[34] S. Mi, T. Wei, J. Sun, P. Liu, X. Li, Q. Zheng, K. Gong, X. Liu, X. Gao, B. Wang, H. Zhao, H. Liu, B. Shen, J. Catal. 347 (2017) 116–126.
[35] D. Verboekend, T.C. Keller, S. Mitchell, J. Pérez-Ramírez, Adv. Funct. Mater. 23 (2013) 1923–1934.
[36] W. Zhou, Y. Zhou, Q. Wei, S. Ding, S. Jiang, Q. Zhang, M. Liu, Chem. Eng. J. 330 (2017) 605–615.
[37] W. Zhou, M. Liu, Q. Zhang, Q. Wei, S. Ding, Y. Zhou, ACS Catal. 7 (2017) 7665–7679.
[38] W. Zhou, Q. Zhang, Y. Zhou, Q. Wei, L. Du, S. Ding, S. Jiang, Y. Zhang, Catal. Today 305 (2018) 171–181.
[39] Q. Cui, Y. Zhou, Q. Wei, X. Tao, G. Yu, Y. Wang, J. Yang, Energy Fuels 26 (2012) 4664–4670.
[40] G. Kupgan, T.P. Liyana-Arachchi, C.M. Colina, Langmuir 33 (2017) 11138–11145.
[41] W. Chen, F. Maugé, J. van Gestel, H. Nie, D. Li, X. Long, J. Catal. 304 (2013) 47–62.
[42] R.A. Ortega-Domínguez, J.A. Mendoza-Nieto, P. Hernández-Hipólito, F. Garrido-Sánchez, J. Escobar-Aguilar, S.A.I. Barri, D. Chadwick, T.E. Klimova, J. Catal. 329 (2015) 457–470.
[43] Y. Fan, H. Xiao, G. Shi, H. Liu, X. Bao, Energy Environ. Sci. 4 (2011) 572–582.
[44] D. Zhang, W.-Q. Liu, Y.-A. Liu, U.J. Etim, X.-M. Liu, Z.-F. Yan, Chem. Eng. J. 330 (2017) 706–717.
[45] L. Díaz-García, V. Santes, T. Viveros-García, A. Sánchez-Trujillo, J. Ramírez-Salgado, C. Ornelas, E. Rodríguez-Castellón, Catal. Today 282 (2017) 230–239.
[46] M. Li, H. Li, F. Jiang, Y. Chu, H. Nie, Catal. Today 149 (2010) 35–39.
[47] P.A. Nikulshin, V.A. Salnikov, A.V. Mozhaev, P.P. Minaev, V.M. Kogan, A.A. Pimerzin, J. Catal. 309 (2014) 386–396.
[48] O.Y. Gutiérrez, S. Singh, E. Schachtl, J. Kim, E. Kondratieva, J. Hein, J.A. Lercher, ACS Catal. 4 (2014) 1487–1499.
[49] B. Pawelec, J.L.G. Fierro, A. Montesinos, T.A. Zepeda, Appl. Catal., B 80 (2008) 1–14.
[50] D. Meloni, D. Perra, R. Monaci, M.G. Cutrufello, I. Rombi, I. Ferino, Appl. Catal., B 184 (2016) 163–173.
[51] R. Nava, A. Infantes-Molina, P. Castaño, R. Guil-López, B. Pawelec, Fuel Lond. (Lond) 90 (2011) 2726–2737.
[52] A. Alsalme, N. Alzaqri, A. Alsaleh, M.R.H. Siddiqui, A. Alotaibi, E.F. Kozhevnikova, I.V. Kozhevnikov, Appl. Catal., B 182 (2016) 102–108.
[53] J. Hein, O.Y. Gutiérrez, S. Albersberger, J. Han, A. Jentys, J.A. Lercher, ChemCatChem 9 (2017) 629–641.
[54] Z. Cao, A. Duan, Z. Zhao, J. Li, Y. Wei, G. Jiang, J. Liu, J. Mater. Chem. A 2 (2014) 19738–19749.
[55] F.Y. Cheng, J. Chen, X.L. Gou, Adv. Mater. 18 (2006) 2561–2564.
[56] J. Lauritsen, J. Kibsgaard, G. Olesen, P. Moses, B. Hinnemann, S. Helveg, J. Norskov, B. Clausen, H. Topsoe, E. Lagsgaard, J. Catal. 249 (2007) 220–233.
[57] N.-Q. Bui, C. Geantet, G. Berhault, J. Catal. 330 (2015) 374–386.
[58] D. Ishutenko, P. Minaev, Y. Anashkin, M. Nikulshina, A. Mozhaev, K. Maslakov, P. Nikulshin, Appl. Catal., B 203 (2017) 237–246.
[59] F. Pelardy, A.S. dos Santos, A. Daudin, E. Devers, T. Belin, S. Brunet, Appl. Catal., B 206 (2017) 24–34.
[60] Y. Zu, Y. Qin, X. Gao, H. Liu, X. Zhang, J. Zhang, L. Song, Appl. Catal., B 203 (2017) 96–107.
[61] P. Yuan, J. Liu, Y. Li, Y. Fan, G. Shi, H. Liu, X. Bao, Chem. Eng. Sci. 111 (2014) 381–389.
[62] L. van Haandel, G.M. Bremmer, E.J.M. Hensen, T. Weber, J. Catal. 351 (2017) 95–106.
[63] H. Zhu, W. Guo, M. Li, L. Zhao, S. Li, Y. Li, X. Lu, H. Shan, ACS Catal. 1 (2011) 1498–1510.